PNAS RESEARCH ARTICLE | NEUROSCIENCE

Structural and functional reorganization of inhibitory synapses by activity-dependent cleavage of neuroligin-2

Na Xu[a,b,c,1], Ran Cao[b,d,1], Si-Yu Chen[c,d], Xu-Zhuo Gou[b,c,d], Bin Wang[b,e], Hong-Mei Luo[b,c], Feng Gao[a], and Ai-Hui Tang[a,b,c,d,2]

Edited by Yishi Jin, University of California San Diego, La Jolla, CA; received August 23, 2023; accepted March 21, 2024

Recent evidence has demonstrated that the transsynaptic nanoscale organization of synaptic proteins plays a crucial role in regulating synaptic strength in excitatory synapses. However, the molecular mechanism underlying this transsynaptic nanostructure in inhibitory synapses still remains unclear and its impact on synapse function in physiological or pathological contexts has not been demonstrated. In this study, we utilized an engineered proteolysis technique to investigate the effects of acute cleavage of neuroligin-2 (NL2) on synaptic transmission. Our results show that the rapid cleavage of NL2 led to impaired synaptic transmission by reducing both neurotransmitter release probability and quantum size. These changes were attributed to the dispersion of RIM1/2 and $GABA_A$ receptors and a weakened spatial alignment between them at the subsynaptic scale, as observed through superresolution imaging and model simulations. Importantly, we found that endogenous NL2 undergoes rapid MMP9-dependent cleavage during epileptic activities, which further exacerbates the decrease in inhibitory transmission. Overall, our study demonstrates the significant impact of nanoscale structural reorganization on inhibitory transmission and unveils ongoing modulation of mature GABAergic synapses through active cleavage of NL2 in response to hyperactivity.

mature synapse | synaptic transmission | synaptic adhesion molecule | neuroligin-2 | STORM

Significance

Our study provides significant insights into the role of transsynaptic nanoalignment in modulating synaptic strength, particularly in inhibitory synapses. Through modeling and superresolution imaging, we demonstrate the critical role of neuroligin-2 (NL2) in organizing nanocolumns in GABAergic synapses and its impact on synaptic transmission when acutely disrupted. Furthermore, our research highlights the ongoing modulation of established inhibitory synapses through MMP9-mediated cleavage of NL2 during epileptic activities. These findings shed light on the significance of nanoarchitecture in synaptic function and provide a unique understanding of the ongoing role of NL2 in established inhibitory synapses.

Organizational protein complexes play central roles both in orchestrating synapse formation and in defining the functional properties of synaptic transmission that together shape the flow of information through neuronal networks (1). Recent work suggests that nanoscale organization of the proteins within synapses has substantial impacts on synapse function (2). Specifically, active zone scaffold proteins, including the regulating synaptic membrane exocytosis protein (RIM) (3) and Munc13 (4), form nanoclusters that define sites of neurotransmitter release, and these sites align transsynaptically with clustered postsynaptic receptors (5, 6) to form an organization referred to as a nanocolumn (3, 7–9). Numerical models have demonstrated that receptor activation strongly depends on its distance to the site of neurotransmitter release (10, 11). Accumulating superresolution imaging data, mainly in excitatory synapses, have demonstrated an essential role of nanoscale reorganization of synaptic proteins in modulating synaptic transmission (12–15). However, these pieces of evidence are based on either knockout or knockdown of key synaptic proteins such as neuroligins (12, 13) or proteolytically cleavage of engineered LRRTM2 that does not undergo proteolytic cleavage endogenously. Thus, evidence is still lacking for the nanostructural reorganization-mediated modulation of synaptic strength in neurons under physiological or pathological conditions.

Multiple transsynaptic adhesion molecules have been identified to be necessary for the maintenance of nanocolumns in glutamatergic synapses, including neuroligin-1 (13), neuroligin-3 (12), LRRTM2 (15), and Cbln (16). Likewise, GABAergic synapses also possess transsynaptic nanocolumns that align subsynaptic nanoclusters of GlyRs and $GABA_A$Rs to those of RIM1/2 (7, 17). However, studies on the molecular mechanisms of nanocolumn maintenance in inhibitory synapses are lacking. Neuroligins form transsynaptic bridges by binding presynaptic neurexins to regulate various aspects of excitatory and inhibitory synaptic transmission (18–20). Neuroligin-2 (NL2) is the only member that acts exclusively at GABAergic inhibitory synapses (21–25), with its intracellular domain interacting with the scaffolding protein gephyrin that anchors γ-aminobutyric acid subtype A receptors ($GABA_A$Rs) (22, 26). Therefore, NL2 represents a strong candidate to mediate transsynaptic alignment in GABAergic synapses.

The effects of NL2 on the genesis and development of inhibitory synapses have been well documented (20, 21, 23, 27, 28). Altered expression or mutations of NL2 and several of its interacting partners are linked to cognitive and psychiatric disorders, including epilepsy, schizophrenia, autism, and anxiety (29). Recent evidence has also suggested that NL2 plays essential roles during adulthood in synapse maintenance. Conditional deletion

Author contributions: N.X., R.C., and A.-H.T. designed research; N.X., R.C., S.-Y.C., X.-Z.G., H.-M.L., and F.G. performed research; B.W. contributed new reagents/analytic tools; N.X. and R.C. analyzed data; and N.X., R.C., and A.-H.T. wrote the paper.

The authors declare no competing interest.

This article is a PNAS Direct Submission.

[1]N.X. and R.C. contributed equally to this work.

[2]To whom correspondence may be addressed. Email: tangah@ustc.edu.cn.

This article contains supporting information online at https://www.pnas.org/lookup/suppl/doi:10.1073/pnas.2314541121/-/DCSupplemental.

Published April 24, 2024.

of NL2 in the medial prefrontal cortex (30) or lateral septum (31) in adult mice results in reduced synaptic transmission of inhibitory synapses. However, these studies cannot distinguish the ongoing role of NL2 molecules themselves from the secondary effects of the substantial and complex compensation apparent during the weeks for NL2 deletion to take effect. The exact ongoing role of NL2 in established inhibitory synapses is still obscure.

In the current study, we engineered a tagged NL2 with a proteolytic cleavage site so that we could acutely disrupt its extracellular interactions with proteolysis on demand. We found that acute cleavage of NL2 led to impaired inhibitory synaptic transmission, which resulted from a reduction in both presynaptic neurotransmitter release probability and postsynaptic quantum size. Using STORM superresolution imaging, we found that NL2 cleavage led quickly to a more diffuse distribution of $GABA_A$Rs and an impaired nanoscale enrichment of $GABA_A$Rs to the presynaptic release sites without altering the overall receptor retention at synapses. A numerical model incorporating these structural changes fully predicted the electrophysiological findings. More importantly, in response to epileptic activity, endogenous NL2 underwent MMP-9-dependent cleavage, resulting in decreased inhibitory synaptic transmission as expected. Therefore, our study reveals mechanisms for the modulation of synaptic transmission by NL2 at mature inhibitory synapses, characterizes the detailed modulation of synaptic function by various nanoscale reorganizations of synaptic proteins, and provides evidence for the causation of synaptic dysfunction by acute structural reorganization in response to hyperactivity.

Results

Acute and Specific Cleavage of the NL2 Extracellular Domain. To examine the impact of NL2 extracellular interactions on mature synapses, we utilized a method where a short recognition sequence for the enzyme thrombin was inserted at an extracellular juxtamembrane position within NL2. This allowed for the specific cleavage of the extracellular domain in response to thrombin application (32) (Fig. 1*A*). Meanwhile, we appended enhanced green fluorescent protein to the N-terminus of NL2 to visualize and measure the cleavage of NL2 in live neurons. By replacing endogenous NL2 (27) with engineered GFP-NL2 or GFP-NL2-Thr, we found that GFP-NL2-Thr clustered in small puncta that primarily colocalized with inhibitory synapses (Fig. 1 *B–D*). This suggests that the insertion of the thrombin recognition site does not interfere with the synaptic localization of NL2.

To determine whether the insertion of the recognition site affects the synaptogenesis function of NL2, we quantified inhibitory synapses by labeling transfected neurons with antibodies against gephyrin and the $GABA_A$ receptor γ2 subunit (*SI Appendix*, Fig. S1*A*). Consistent with previous studies (24, 33, 34), knockdown of NL2 significantly reduced both the puncta size and density of gephyrin and $GABA_A$R, while overexpression of GFP-NL2-thr led to an increase in the puncta density of gephyrin and $GABA_A$R compared with scrambled shRNA controls (*SI Appendix*, Fig. S1 *A–E*). This indicates that the insertion of the thrombin recognition site does not disrupt the synaptogenesis function of NL2. Furthermore, when shNL2 and GFP-NL2-Thr were coexpressed, there was no change in the size or density of $GABA_A$R or gephyrin, suggesting that the expression level of GFP-NL2-Thr was comparable to that of the endogenous protein (*SI Appendix*, Fig. S1 *A–E*).

To test whether GFP-NL2-Thr can be acutely cleaved by thrombin, hippocampal neurons were transfected with plasmids encoding shNL2 and GFP-NL2 or GFP-NL2-Thr, and the GFP fluorescence was monitored with live imaging. After the addition of thrombin, the fluorescence intensity of neurons expressing GFP-NL2-Thr decreased rapidly, while there was no change in the intensity of GFP-NL2 (Fig. 1 *E–G*). These results demonstrate that replacing endogenous NL2 with GFP-NL2-Thr allows for the acute and specific cleavage of the extracellular domain of NL2.

Acute NL2 Cleavage Decreases Miniature Inhibitory Synaptic Transmission. Traditional manipulations of NL2, such as knockdown or knockout, can lead to developmental deficits or compensatory effects, making it difficult to understand its role in mature synapses. However, by using GFP-NL2-Thr for acute and specific cleavage of the protein, we were able to directly assess the impact of NL2 disruption on synaptic transmission. Whole-cell patch clamp recordings were performed on cultured rat hippocampal neurons cotransfected with shNL2 and either GFP-NL2 or GFP-NL2-Thr. We also used neurons expressing shNL2 and GFP-NL2 without a thrombin cleavage site as controls for potential off-target effects.

When recording miniature inhibitory postsynaptic currents (mIPSCs, Fig. 2 *A* and *B*), we found that thrombin had no significant effect on the frequency (Fig. 2 *C* and *D*) or amplitude (Fig. 2 *G* and *H*) in neurons expressing shNL2 and GFP-NL2. However, in neurons expressing shNL2 and GFP-NL2-Thr, thrombin application led to a significant decrease in both the frequency (by 67.6%, Fig. 2 *E* and *F*) and amplitude (by 10.9%, Fig. 2 *I* and *J*) of mIPSCs. These data suggest that acute cleavage of NL2 ECD rapidly leads to a reduction in synaptic transmission of GABAergic synapses, possibly by affecting both pre- and postsynaptic compartments. Additionally, after NL2 was cleaved, no significant difference was found between kinetics of mEPSCs (*SI Appendix*, Fig. S3 *A–N*) and the rise time of mIPSCs, while the decay time of mIPSCs was reduced (*SI Appendix*, Fig. S2 *A–E*). Therefore, acute cleavage of NL2 exerts a specific effect on inhibitory GABAergic synapses but not on excitatory synapses, consistent with the primary localization of NL2 in GABAergic synapses (23, 24).

Acute NL2 Cleavage Decreases AP-Dependent Inhibitory Synaptic Transmission. Evidence shows that spontaneous and action-potential (AP)-evoked transmitter release differ in terms of release sites and activated postsynaptic receptors (3, 35). To examine the effect of NL2 cleavage on AP-evoked synaptic transmission, we performed whole-cell patch clamp recordings on neurons transfected with shNL2 and either GFP-NL2-Thr or GFP-NL2. Ten trials of IPSCs were recorded before and 20 min after thrombin application (Fig. 3*A*). In neurons expressing shNL2 and GFP-NL2, thrombin had no effect on the amplitude of the first IPSCs (Fig. 3*B*) or the paired-pulse ratio (PPR, Fig. 3*C*). However, in neurons expressing shNL2 and GFP-NL2-Thr, thrombin treatment significantly reduced the amplitude of the first response (by 52.8%, Fig. 3*B*) and increased the PPR (by 18.3%, Fig. 3*C*). When two pulses are paired in quick succession, the relative amplitude of the second peak is thought be a tradeoff between the facilitating residual Ca^{2+} and the depressing vesicle depletion, both taking place in presynaptic terminals; therefore, changes in PPR have been interpreted to reflect presynaptic changes in release probability (Pr) (36). These results strongly suggest that NL2 cleavage decreases the presynaptic release probability of GABA.

We also performed multiple-probability fluctuation analysis (MPFA) to quantify the quantal parameters of transmission at these synapses (Fig. 3*D*) (37). Neither release probability, quantal size, or synapse number were changed by thrombin application by thrombin application in neurons expressing shNL2 and GFP-NL2 (Fig. 3 *E–G*), suggesting that there is no unspecific effect of thrombin on GABAergic synaptic transmission. However,

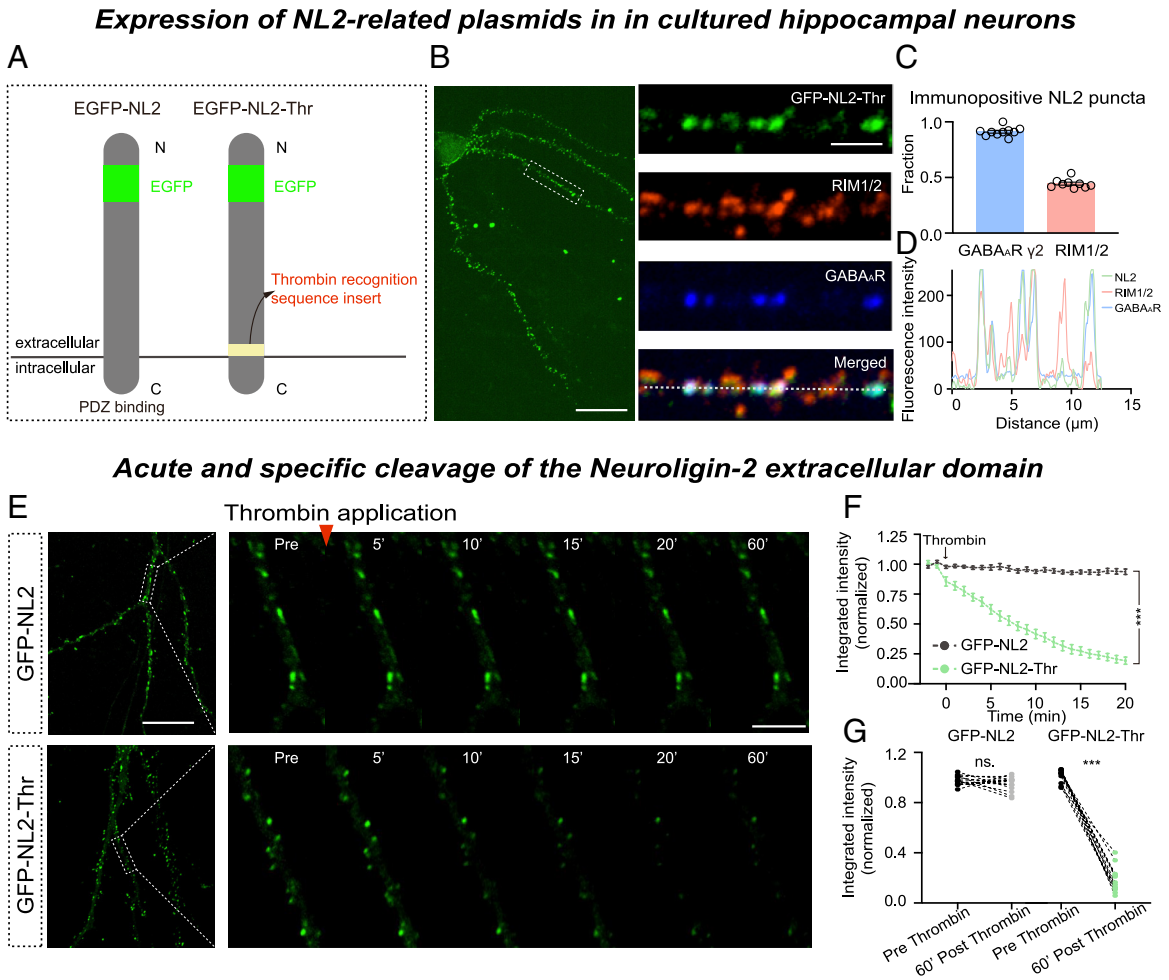

Fig. 1. Acute and specific cleavage of the NL2 extracellular domain. (*A*) The structural diagram of GFP-NL2 (*Left*) and GFP-NL2-Thr (*Right*). The yellow area represents the thrombin recognition sequence. (*B*) Representative expression images of GFP-NL2-Thr in cultured hippocampal neurons and immunostaining of endogenous $GABA_AR$ and RIM1/2 visualized by confocal microscopy. The white dotted box on the left is region of interest. [Scale bar, 30 μm (*Left*) and 10 μm (*Right*).] (*C*) Quantification of the colocalization between expressed GFP-NL2-Thr, $GABA_AR$, and RIM1/2. $GABA_AR$, n = 10 cells; RIM1/2, n = 9 cells. (*D*) Fluorescence intensity along dotted line in (*B*). (*E*) Representative images from a confocal time series of GFP-NL2 and GFP-NL2-Thr cleavage following thrombin application (red arrow; 10 U/mL). [Scale bar, 30 μm (*Left*) and 10 μm (*Right*).] (*F*) Quantification of GFP-NL2 and GFP-NL2-Thr cleavage. GFP-NL2, n = 13 cells; GFP-NL2-Thr, n = 12 cells. $F_{(1,23)} = 210.8000$, $P < 0.0001$. (*G*) Quantification of GFP-NL2 and GFP-NL2-Thr before and after 1 h thrombin cleavage. GFP-NL2, n = 13 cells, $P = 0.1818$, t = 1.4170; GFP-NL2-Thr, n = 12 cells, $P < 0.0001$. All data are presented as the mean ± SEM. *$P < 0.05$, **$P < 0.01$, ***$P < 0.001$. Significance was assessed by two-way ANOVA with repeated measures (*F*) and paired *t* test (*G*).

in neurons expressing shNL2 and GFP-NL2-Thr (Fig. 3*H*), thrombin significantly reduced the release probability (by 18.7%, Fig. 3*I*) and quantum size (by 27.5%, Fig. 3*J*), while the synapse number remained the same (Fig. 3*K*). These analyses suggest that acute cleavage of NL2 decreases inhibitory synaptic transmission by reducing both presynaptic release probability and postsynaptic quantum size.

Cleavage of Postsynaptic NL2 Restructures the Nano-Organization of Active Zone Proteins and Decreases Pr. Recent super-resolution studies have discovered that both pre- and postsynaptic properties depend on nanoscale organizations of key synaptic proteins (3, 6, 38). RIM1/2 forms nanoclusters to guide release and interacts with Ca^{2+} channels to define release sites (3, 39). Our study examined the effect of NL2 cleavage on these properties using dSTORM imaging. $GABA_ARs$ and RIM1/2 were labeled with antibodies against the $GABA_AR$ γ2 subunit and RIM1/2, respectively after thrombin incubation. Confocal imaging uncovered no marked changes in either the degree of overlap between RIM1/2 and $GABA_AR$ (Fig. 4 *A* and *B*) or their fluorescent intensities (Fig. 4 *C* and *D*), suggesting that cleavage of NL2 does not alter the overall presynaptic retention of RIM1/2. With STORM imaging (Fig. 4 *E* and *F*), we found that inhibitory synapses with NL2 cleaved were larger in the volumes of RIM1/2 synaptic clusters (by 61.2%) and lower in overall localization density (by 35.2%) within clusters (Fig. 4 *H* and *I*). At the subsynaptic level, the cleavage of NL2 increased the RIM1/2 nanocluster number per synapse (by 22.5%, Fig. 4*G*) as well as their volume (by 36.7%, Fig. 4*J*) and decreased the localization density within nanoclusters (by 30.8%, Fig. 4*K*). These results suggest that the cleavage of NL2 makes RIM1/2 distribute more diffusely within active zones.

To test whether the cleavage of NL2 leads to changes in the subsynaptic distribution of P/Q-type Ca^{2+} channels, CaV2.1 puncta were analyzed (*SI Appendix*, Fig. S4*A*). The cleavage of NL2 did not change the fractions of CaV2.1 and $GABA_AR$ puncta that colocalized with each other (*SI Appendix*, Fig. S4*B*) or their puncta sizes (*SI Appendix*, Fig. S4 *C* and *D*). Under STORM resolution, we also found no significant differences in synaptic cluster volume, localization density within synaptic clusters, nanocluster volume, or density within nanoclusters for CaV2.1 between synapses with and without NL2 cleavage (*SI Appendix*, Fig. S4 *E–O*). Together, our results demonstrate that the cleavage of postsynaptic

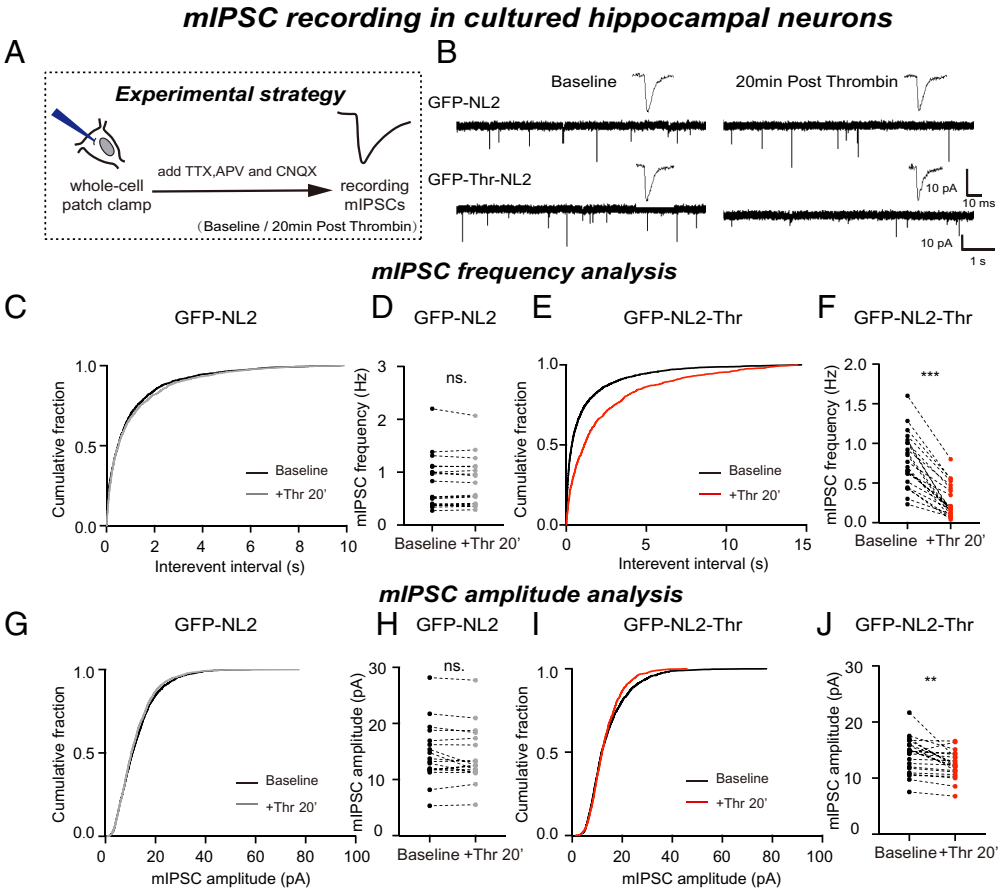

Fig. 2. Acute cleavage of NL2 rapidly reduces mIPSC frequency and amplitude. (*A*) Schematic of mIPSC experiments. (*B*) Representative traces of mIPSCs recordings from cultured hippocampal neurons transfected with shNL2 and GFP-NL2 or GFP-NL2-Thr before and after the application of thrombin. (Scale bar, 10 pA, 1 s.) *Top*, examples of mIPSC. (Scale bar, 10 pA, 10 ms.) (*C* and *D*) Cumulative fraction (*C*) of interevent interval and the pooled mIPSCs frequency. (*D*) From cultured hippocampal neurons transfected with shNL2 and GFP-NL2 before (black) and after (gray) application of thrombin. n = 18 cells. (*D*), $P = 0.6142$. (*E* and *F*) Cumulative fraction (*E*) of interevent interval and the pooled mIPSCs frequency. (*F*) from cultured hippocampal neurons transfected with shNL2 and GFP-NL2-Thr before (black) and after (gray) application of thrombin. n = 22 cells. (*D*), $P < 0.0001$. (*G* and *H*) Cumulative fraction (*G*) of interevent interval and the pooled mIPSCs amplitude. (*H*) from cultured hippocampal neurons transfected with shNL2 and GFP-NL2 before (black) and after (gray) application of thrombin. n = 18 cells. (*D*), $P = 0.1262$. (*I* and *J*) Cumulative fraction (*I*) of interevent interval and the pooled mIPSCs frequency. (*J*) from cultured hippocampal neurons transfected with shNL2 and GFP-NL2-Thr before (black) and after (gray) application of thrombin. n = 22 cells. (*D*), $P = 0.0015$. All data are presented as the mean ± SEM. $*P < 0.05$, $**P < 0.01$, $***P < 0.001$. Significance was assessed with the paired *t* test.

NL2 impairs the tight local organization of RIM1/2 within active zones that are critical for fast transmitter release.

Acute NL2 Cleavage Has No Effect on Synaptic Retention of Postsynaptic Proteins. We next set out to assess the structural mechanisms underlying the changes in postsynaptic responses. NL2 has been shown to drive clustering of the postsynaptic gephyrin scaffold, which in turn stabilizes $GABA_A$Rs at GABAergic synapses (28). We first examined the synaptic retention of gephyrin and $GABA_A$Rs in response to cleavage of NL2 by cotransfecting neurons with shNL2 and GFP-NL2-Thr or GFP-NL2 together with a plasmid encoding an RFP-tagged recombinant intrabody against gephyrin (Gephyrin.FingR) (40). We found that the fluorescence intensity of Gephyrin.FingR in synapses remained constant within 60 min after thrombin application (*SI Appendix*, Fig. S5 *A* and *B*). With longer incubation time, the average size, fluorescence intensity, and puncta density of Gephyrin.FingR puncta were significantly reduced in cultures incubated for 12 h or longer (*SI Appendix*, Fig. S6 *A–D*). These results suggest that while long-term disruption of NL2-dependent interactions results in the disassembly of gephyrin puncta, NL2 integrity is not required for the synaptic retention of gephyrin in established synapses within a 1-h time window.

To examine the synaptic retention of $GABA_A$Rs, we labeled $GABA_A$Rs in neurons fixed at different time points after thrombin application. Only the $GABA_A$R puncta colocalized with GFP-NL2 or GFP-NL2-Thr were analyzed. Similar to gephyrin, at 20 or 60 min after thrombin application, $GABA_A$Rs did not show any changes in either puncta size or puncta density along dendrites in neurons expressing either GFP-NL2 or GFP-NL2-Thr (*SI Appendix*, Fig. S5 *C–E*); when incubated for a longer time, both the size and density of $GABA_A$R puncta were significantly reduced in neurons expressing GFP-NL2-Thr (*SI Appendix*, Fig. S6 *E–H*). These data suggest that the NL2 ECD is not required for short-term retention of $GABA_A$Rs at synapses.

Since NL2 is exclusively localized in GABAergic synapses (23), disruption of NL2 is expected to have no effect on glutamatergic synapses. This was tested by imaging an RFP-tagged recombinant intrabody against PSD-95 (PSD95.FingR) (40) (*SI Appendix*, Fig. S7*A*). As predicted, no significant changes were found in puncta size, fluorescence intensity, or puncta density (*SI Appendix*, Fig. S7 *B–D*) of PSD95.FingR after thrombin incubation. These results suggest that acute disruption of NL2 ECD does not alter the morphology of excitatory synapses. Taken together, these data demonstrate that acute cleavage of the ECD of engineered NL2 does not rapidly lead to a reduction in synaptic retention of key postsynaptic molecules, including gephyrin and $GABA_A$Rs.

Cleavage of Postsynaptic NL2 Reorganizes the Subsynaptic Distributions of $GABA_A$R and Gephyrin. In excitatory synapses, AMPA receptors form local high-density nanoclusters (5, 41) and their reorganization can efficiently modulate the synaptic strength (6, 15). $GABA_A$Rs have been shown to form similar nanoscale organizations (42). We therefore speculate that cleavage of NL2 may lead to the reorganization of $GABA_A$R distribution, which in turn results in reduced quantal size. To test this, we examined the subsynaptic $GABA_A$R distributions with STORM (Fig. 5 *A* and *B*). We found that synaptic clusters of $GABA_A$Rs in GFP-NL2-Thr-expressing neurons had an increased volume (by 39.3%) and a decreased overall protein density (by 27.2%) compared with those in GFP-NL2-expressing neurons (Fig. 5 *D–G*). At the subsynaptic level, while synapses with and without NL2 cleaved had a similar number of $GABA_A$R nanoclusters

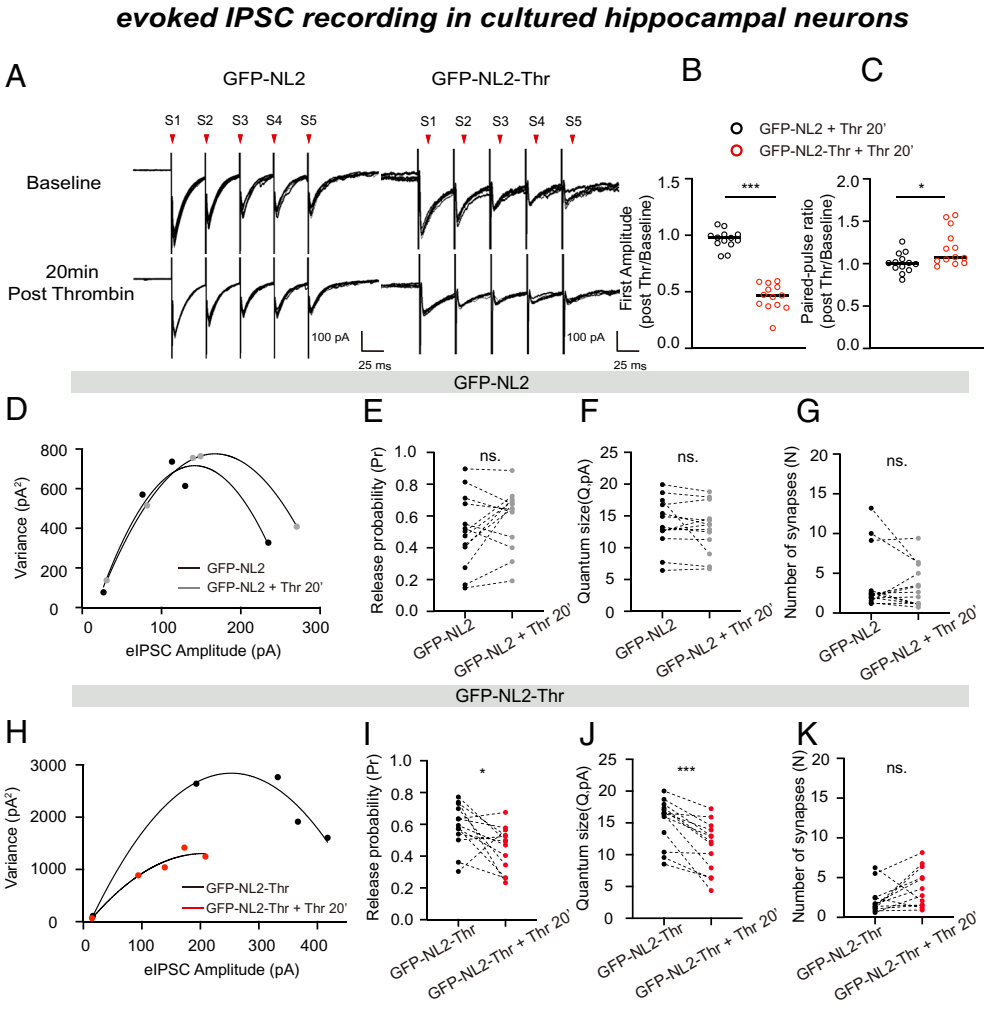

Fig. 3. NL2 cleavage rapidly reduces inhibitory synaptic transmission. (*A*) IPSCs were triggered by five pulses with a 50 ms interval. Example traces of 10 overlapping synaptic responses from neurons transfected with shNL2 and GFP-NL2 or GFP-NL2-Thr before and after the application of thrombin. The red arrow represents the stimulus. [Scale bar (*Left*), 100 pA, 25 ms.] [Scale bar (*Right*), 200 pA, 25 ms.] (*B*) eIPSC first amplitude change before and after thrombin incubation in neurons expressing GFP-NL2 or GFP-NL2-Thr. GFP-NL2, n = 13 cells; GFP-NL2-Thr, n = 13 cells, $P < 0.0001$. (*C*) PPR change before and after thrombin incubation in neurons expressing GFP-NL2 or GFP-NL2-Thr. GFP-NL2, n = 13 cells; GFP-NL2-Thr, n = 13 cells, $P = 0.0150$. (*D*) Fitting of the variance-amplitude relation for data from example recordings in (*A*, *Left*). Black and gray represent data from neurons before and after acute application of thrombin, respectively. (*E*–*G*) The release probability (*E*), quantal size (*F*) and number of synapses (*G*) derived from the parabolic fit from GFP-NL2 neurons. n = 13 cells, $P = 0.1183$, 0.2795, and 0.3647. (*H*) Fitting of the variance-amplitude relation for data from example recordings in (*A*, *Right*). Black and red represent data from neurons before and after acute application of thrombin, respectively. (*I*–*K*) The release probability (*I*), quantal size (*J*), and number of synapses (*K*) derived from the parabolic fit from GFP-NL2-Thr neurons. n = 13 cells. (*I*), $P = 0.0241$; (*J*) $P < 0.0001$; (*K*) $P = 0.3647$. All data are presented as the mean ± SEM. *$P < 0.05$, **$P < 0.01$, ***$P < 0.001$. Significance was assessed with the paired *t* test.

(Fig. 5*C*), the $GABA_AR$ nanoclusters in NL2-cleaved synapses had a larger volume (by 27.8%) and a lower protein density within nanoclusters (by 35.8%) (Fig. 5 *F* and *G*). These results demonstrate that acute cleavage of NL2 can rapidly reorganize the distribution of $GABA_ARs$ at both synaptic and subsynaptic scales.

As a central scaffold at inhibitory synapses, gephyrin has been found to play key roles in postsynaptic clustering of glycine receptors and $GABA_ARs$ (43, 44). We therefore wondered whether cleavage of NL2 alters receptor distribution by reorganizing gephyrin. To test this, we quantitatively analyze the nanoscale organization of gephyrin. The results showed that the distribution of gephyrin changed in a very similar manner to that of $GABA_ARs$ in response to the cleavage of NL2 (*SI Appendix*, Fig. S8). Together, these data demonstrate a dramatically more diffuse distribution of $GABA_ARs$ and gephyrins when NL2 is acutely disrupted, suggesting an essential role of NL2 in maintaining postsynaptic nanoscale organization in GABAergic synapses.

NL2 Enriches $GABA_ARs$ to Presynaptic RIM-Defined Neurotransmitter Release Sites. In excitatory synapses, presynaptic sites of glutamate release, as marked by RIM nanoclusters, are aligned with postsynaptic AMPAR nanoclusters within nanocolumns (3), and disruption of this alignment leads to reduced postsynaptic current in response to AP-evoked transmitter release (13, 15). Nanocolumns have also been found in inhibitory synapses (7). We therefore speculate that NL2 may participate in the organization of nanocolumns and that cleavage of NL2 may reduce the quantal size (Fig. 3*J*) of evoked GABAergic transmission by disrupting the nanocolumn. To test this, we first examined whether NL2 is enriched in nanocolumns. The transsynaptic alignment between RIM1/2 and $GABA_ARs$ was quantified with the local protein enrichment assay (3, 45). These two proteins were mutually enriched with each other (Fig. 6 *A* and *B*) to form transsynaptic nanocolumns. Moreover, the postsynaptic scaffold gephyrin was also enriched with $GABA_ARs$ (*SI Appendix*, Fig. S8 *H*–*K*). To test how NL2 is distributed relative to nanocolumns, we measured the subsynaptic organization of endogenous NL2 relative to $GABA_ARs$ (Fig. 6 *C* and *D*). As we predicted, NL2 showed significant local enrichment with $GABA_ARs$, suggesting that NL2 is involved in the nanocolumn structure.

We next tested whether the cleavage of NL2 leads to the disruption of transsynaptic nanocolumns. Compared with synapses onto neurons expressing the noncleavable GFP-NL2, synapses with cleaved NL2 showed a marked reduction in local densities of $GABA_ARs$ and RIM1/2 at positions laterally close to the nanoclusters of RIM1/2 and $GABA_ARs$ across the cleft, respectively (Fig. 6 *E*–*G*). To simply summarize the enrichment, we defined an enrichment index as the averaged normalized protein density within 60 nm from the nanocluster center of the other protein (3). Synapses with cleaved NL2 demonstrated a significantly decreased enrichment index (by 16.3% and 15.1% for $GABA_ARs$ and RIM1/2, respectively) compared with synapses expressing noncleavable NL2 (Fig. 6*H*). These data suggest that NL2 contributes to the maintenance of nanocolumns in GABAergic synapses and that its disruption reduces the local enrichment of $GABA_ARs$ to presynaptic release sites defined by RIM1/2 nanoclusters.

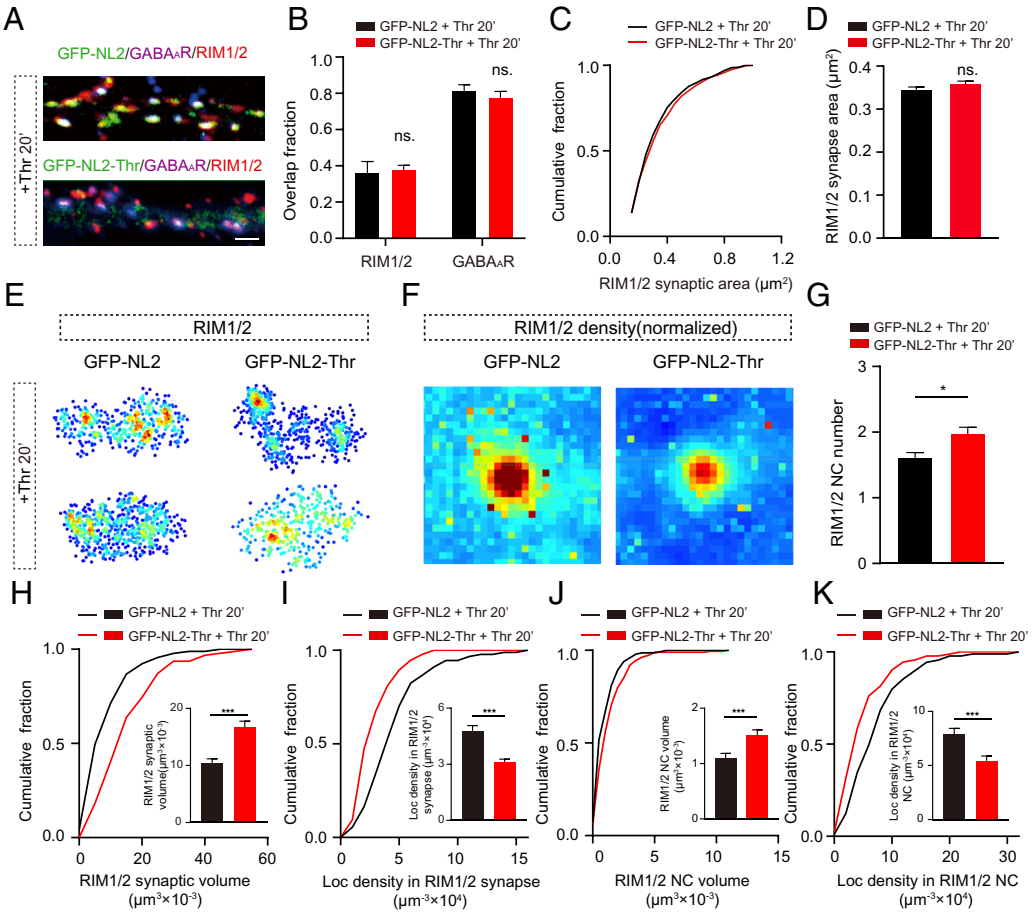

Fig. 4. The cleavage of NL2 causes a significant change in function and organization of presynaptic at inhibitory synapses. (*A*) Representative confocal images of immunocytochemical staining of endogenous RIM1/2 and $GABA_AR$ from neurons expressing GFP-NL2 and GFP-NL2-Thr treated with thrombin. (Scale bar, 2 μm.) (*B*) Quantification of overlap fraction of RIM1/2 and $GABA_A$Rs from confocal images. GFP-NL2, n = 20 cells; GFP-NL2-Thr, n = 19 cells. $P = 0.4115$, $P = 0.1021$; Mann–Whitney test. (*C* and *D*) Analyses of RIM1/2 puncta area from confocal images. GFP-NL2, n = 522 synapses; GFP-NL2-Thr, n = 522 synapses. $P = 0.3957$. (*E*) En-face (*Top*) and side (*Bottom*) views of synaptic RIM1/2 local density maps by STORM imaging in neurons expressing GFP-NL2 (*Left*) or GFP -NL2-Thr (*Right*) treated with thrombin. (Scale bar, 100 nm.) (*F*) Representation of RIM1/2 density averaged across synapses. (Scale bar, 100 nm.) (*G*) Average number of RIM1/2 nanocluster per synapse in neurons expressing GFP -NL2 (black) or GFP -NL2-Thr (red) treated with thrombin. GFP-NL2, n = 91 synapses; GFP-NL2-Thr, n = 95 synapses. $P = 0.0113$. (*H* and *I*) Analyses of RIM1/2 synaptic cluster volume (*H*; GFP-NL2, n = 91 synapses; GFP-NL2-Thr, n = 94 synapses. $P < 0.0001$) and local density in the synaptic cluster (*I*; GFP-NL2, n = 91 synapses; GFP-NL2-Thr, n = 95 synapses. $P < 0.0001$). (*J* and *K*) Analyses of RIM1/2 nanocluster volume (*J*; GFP-NL2, n = 147 nanoclusters; GFP-NL2-Thr, n = 185 nanoclusters. $P = 0.0005$.) and local density in nanocluster (*K*; GFP-NL2, n = 89 synapses; GFP-NL2-Thr, n = 92 synapses. $P = 0.0001$). All data are presented as the mean ± SEM. $*P < 0.05$, $**P < 0.01$, $***P < 0.001$. Significance was assessed with the Mann–Whitney test (*C*–*K*).

Diluting Distribution of Receptors and Release-Receptor Misalignment Contribute Differently to Reduction in Quantal Size in Model Simulation. To test the functional impact of the observed changes in the nanoscale organization of $GABA_A$Rs, we used Monte Carlo simulations of receptor opening in response to the exocytosis of a single GABA-containing vesicle in a structurally constrained model of an inhibitory synapse. We assumed that action potential–triggered vesicle fusions that mediate single synapse eIPSCs are localized to $GABA_A$R nanoclusters and that spontaneous vesicle fusions that mediate mIPSCs happen randomly over the $GABA_A$R synaptic clusters (3, 15).

We then tested how the changes in the subsynaptic organization of $GABA_A$Rs affect the inhibitory postsynaptic current. We assumed there were 100 $GABA_A$Rs per synapse, with 20 receptors associated with the 80-nm-diameter nanocluster and 80 distributed randomly throughout the 600-nm-diameter PSD (Fig. 6*I*). We first tested the impact of PSD expansion on transmission by increasing the radius of both the nanocluster and synaptic cluster by 25% or 50%, respectively. We found that the eIPSC amplitude was reduced by 17.3% or 26.6% (Fig. 6 *J* and *L*), and the mIPSC amplitude was reduced to a similar extent by 12.7% or 26.7%, respectively (Fig. 6 *K* and *L*). We then examined the impact of nanoscale release-receptor enrichment on the synaptic strength by redistributing 50% or 100% (10 or 20) nanocluster-associated receptors randomly throughout the PSD (Fig. 6*M*). Compared with the original configuration, reducing nanocluster-associated receptors by 50% and 100% decreased the amplitudes of eIPSCs by 14.1% and 28.1%, respectively (Fig. 6 *N* and *P*), but did not change the mIPSC amplitudes (Fig. 6 *O* and *P*). These results demonstrate that diluting the distribution of receptors and release-receptor misalignment have distinct impacts on the amplitudes of mIPSCs and eIPSCs.

Our STORM results revealed a 39.4% expansion in the volumes of $GABA_A$R clusters (Fig. 5*D*) and a 45.3% reduction in the local enrichment of $GABA_A$R to RIM1/2 nanoclusters after acute cleavage of NL2 (Fig. 6*F*). These changes were equivalent to a 22% increase in cluster diameters and removal of 9 receptors from nanoclusters in our model, respectively (Fig. 6*Q*). The simulation predicted that these structural changes resulted in a more pronounced reduction in eIPSC amplitudes (by 29.1%, Fig. 6 *R* and *T*) than in mIPSC amplitudes (by 17.5%, Fig. 6 *S* and *T*). These changes were consistent with the 27.5% and 10.9% reductions in evoked quantal size (Fig. 3*J*) and mIPSC amplitudes (Fig. 2*J*), respectively. Taken together, our model simulation and experimental results suggest

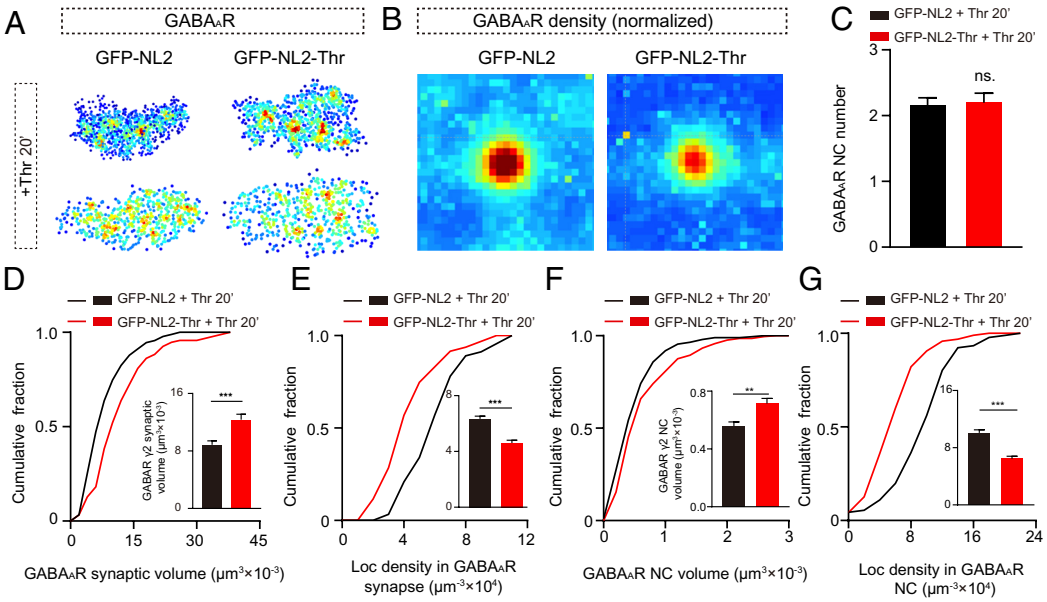

Fig. 5. Acute cleavage of NL2 ECD had no effects on GABAergic postsynaptic complex. (*A*) En-face (*Top*) and side (*Bottom*) views of synaptic $GABA_AR$ local density maps in neurons expressing GFP-NL2 (*Left*) or GFP-NL2-Thr (*Right*). (Scale bar, 100 nm.) (*B*) Representation of $GABA_AR$ density averaged across synapses. (Scale bar, 100 nm.) (*C*) Average number of $GABA_AR$ nanocluster per synapse in neurons expressing GFP-NL2 (black) or GFP-NL2-Thr (red). GFP-NL2, n = 91 synapses; GFP-NL2-Thr, n = 95 synapses. $P = 0.6796$. (*D* and *E*) Analyses of $GABA_AR$ synaptic cluster volume (*D*; GFP-NL2, n = 91 synapses; GFP-NL2-Thr, n = 94 synapses. $P < 0.0001$) and local density in the synaptic cluster (*E*; GFP-NL2, n = 91 synapses; GFP-NL2-Thr, n = 95 synapses. $P < 0.0001$). (*F* and *G*) Analyses of $GABA_AR$ nanocluster volume (*F*; GFP-NL2, n = 197 nanoclusters; GFP-NL2-Thr, n = 208 nanoclusters. $P = 0.0022$) and local density in nanocluster (*G*; GFP-NL2, n = 87 synapses; GFP-NL2-Thr, n = 91 synapses. $P < 0.0001$). All data are presented as the mean ± SEM. $^*P < 0.05$, $^{**}P < 0.01$, $^{***}P < 0.001$. Significance was assessed with the Mann–Whitney test (*C*–*G*).

that diluting the distribution of receptors and release-receptor misalignment both lead to reduced transmission but impact the quantal size of evoked and spontaneous release differently.

NL2 Ectodomain Cleavage by MMP9 Reduces GABAergic Transmission in an Epileptic Neuron Model. To determine whether the NL2 ectodomain can be cleaved under physiological conditions, we first investigated whether NL2 changes during the induction of epileptic model neurons. When neurons were treated with a magnesium-free extracellular solution for 3 h (Fig. 7*A*), GFP-NL2 fluorescence intensity decreased significantly, and this was blocked by preincubation with the MMP9 inhibitor SB-3CT and partially by a general MMP inhibitor GM6001 (Fig. 7 *B* and *C*). These results indicate that MMP9 may mediate the hydrolysis of NL2 under physiological conditions.

To exclude the possibility that increased neuronal activity reduces NL2 expression, we labeled the extra- and intracellular domains of NL2 with antibodies against GFP and NL2 C-terminus in primary hippocampal neurons expressing GFP-tagged NL2, respectively (Fig. 7*D*). The results show that compared with signals at synapses on neurons expressing GFP-NL2, there was a ~44.5% reduction in the GFP/NL2-C ratio at synapses on neurons expressing GFP-NL2-thr after 20 min incubation with thrombin (Fig. 7*E*). This suggests that the GFP/NL2-C ratio measurement is effective in probing the cleavage of NL2. In neurons expressing GFP-NL2, the Mg^{2+}-free treatment significantly reduced the GFP/NL2-C ratio and this reduction was blocked by preincubation with SB-3CT (Fig. 7 *D* and *E*). These data provide further support on our conclusion that epileptic activity enhances MMP9-mediated cleavage of NL2.

To further test this, we used the antibody targeting C-terminus of NL2 to probe the cleaved fragment of NL2 in immunoblotting of epileptic model neurons. The results show that there were two labeled bands in control conditions, with the protein sizes in line with the full-length and the remaining transmembrane domain/c-tail of NL2 after cleavage, respectively (Fig. 7*F*), suggesting NL2 is undergoing a basal level of cleavage. In response to the Mg^{2+}-free treatment, the fraction of smaller transmembrane domain is significantly increased (Fig. 7*G*), and the fraction of full-length protein is decreased (Fig. 7*G*). This change is greatly suppressed by SB-3CT treatment (Fig. 7 *F* and *G*). These results strongly support our conclusion that MMP9-mediated cleavage of NL2 is enhanced in the epileptic condition. However, the basic properties of $GABA_AR$, such as size and density, were not significantly altered 1 h after induction in the epilepsy neuron model (Fig. 7 *H* and *I*).

Moreover, we recorded evoked IPSCs in response to five-pulsed train stimulations from neurons under the epileptic conditions to quantify the potential changes in synaptic transmission (Fig. 7*J*). Mg^{2+}-free treatment significantly reduced the amplitude of the first response (Fig. 7 *K*, *Left*) and increased the PPR (Fig. 7*K*). This change is greatly suppressed by SB-3CT treatment (Fig. 7 *J* and *K*). To further quantify the quantal parameters of the transmission at these synapses, we performed MPFA and found that Mg^{2+}-free treatment significantly reduced the release probability (by 19.1%, Fig. 7 *M*, *Left*) and quantum size (by 38.2%, Fig. 7 *M*, *Middle*), while the synapse number remained the same (Fig. 7 *M*, *Right*). These changes were greatly suppressed by SB-3CT treatment (Fig. 7 *L* and *M*). The recording of mIPSCs showed that mIPSC frequency and amplitude decreased significantly after 1 h of induction, which was significantly rescued by incubation with SB-3CT (*SI Appendix*, Fig. S9 *A*–*C*). These electrophysiological results support that MMP9-mediated NL2 cleavage is able to efficiently modulate GABAergic transmission.

Finally, to address whether NL2 is undergoing activity-dependent cleavage in hippocampal sections, we performed the immunoblotting of NL2 in tissue lysates. The results show that there were two labeled bands in control conditions (Fig. 7*N*), suggesting NL2 is undergoing a basal level of cleavage in mouse hippocampal tissue. After incubating the brain slices with kainate (KA) for 30 min, the fraction of smaller transmembrane domain was significantly increased (Fig. 7 *O*, *Right*), and the fraction of full-length protein was decreased in tissue preparations (Fig. 7*O*). This change was greatly suppressed by SB-3CT treatment (Fig. 7 *N* and *O*).

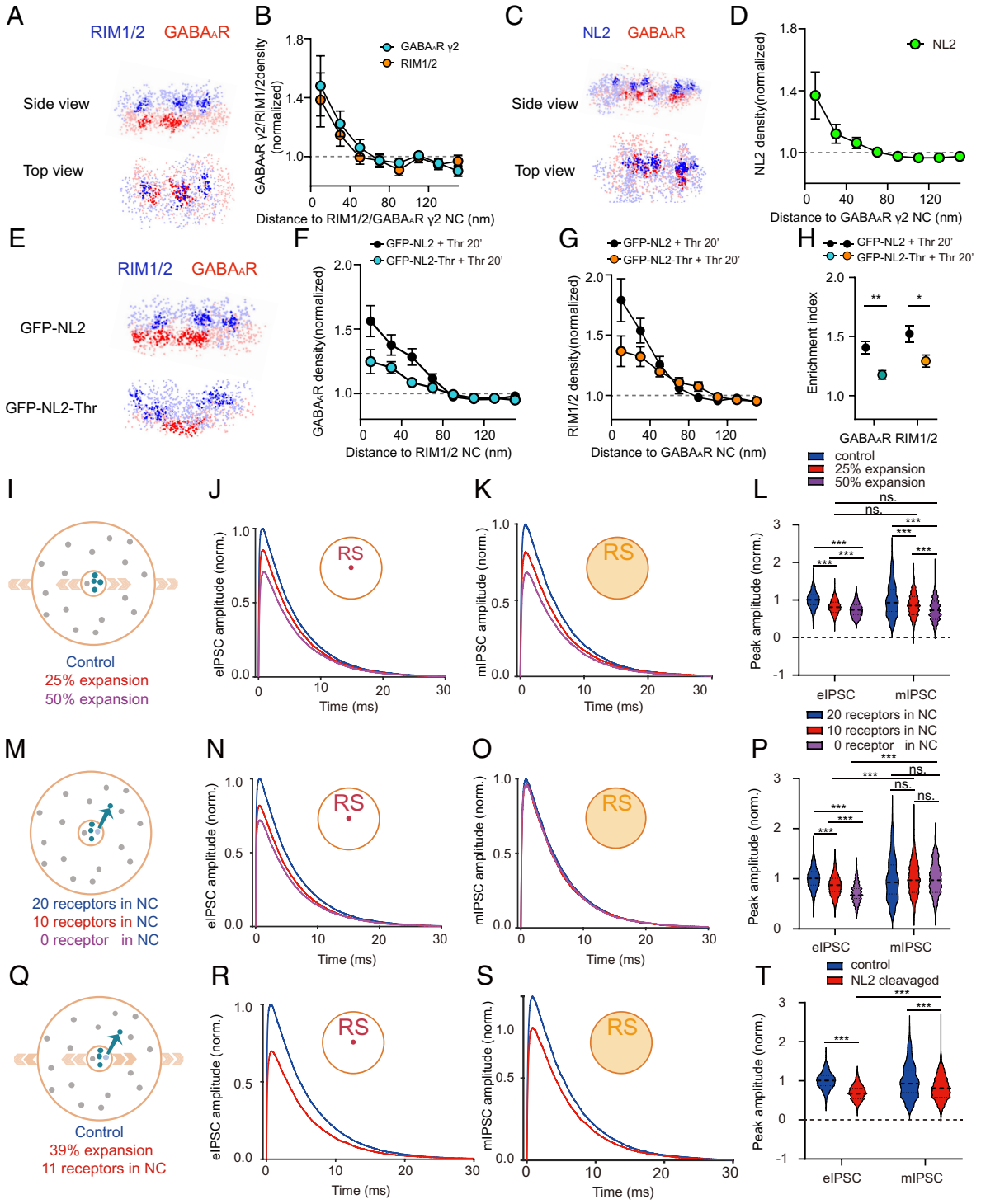

Fig. 6. Numerical model to predict the effects of NL2 loss on synapse function. (*A*) Schematic demonstrating the measurement of 3D coenrichment between protein pairs (RIM1/2, blue; $GABA_AR$, red). En-face (*Top*) and side (*Bottom*) view of the localized positions of $GABA_AR$ (red) and RIM1/2 (blue) with detected nanoclusters indicated in bold. (Scale bar, 100 nm.) (*B*) RIM1/2 protein enrichment as a function of distance from translated $GABA_AR$ centers (orange; 55 nanoclusters) and $GABA_AR$ enrichment relative to RIM1/2 NCs (cyan; 88 nanoclusters). (*C*) Schematic demonstrating the measurement of 3D coenrichment between protein pairs (NL2, blue; $GABA_AR$, red). En-face (*Top*) and side (*Bottom*) view of the localized positions of $GABA_AR$ (red) and NL2 (blue) with detected nanoclusters indicated in bold. (Scale bar, 100 nm.) (*D*) Quantification of NL2 density as a function of the distance to the $GABA_AR$ nanocluster (green; 143 nanoclusters) center. (*E*) Schematic demonstrating the measurement of 3D coenrichment between protein pairs (RIM1/2, blue; $GABA_AR$, red). (*F* and *G*) Quantification of $GABA_AR$ (*F*; GFP-NL2, n = 147 nanoclusters; GFP-NL2-Thr, n = 188 nanoclusters) and RIM1/2 (*G*; GFP-NL2, n = 197 nanoclusters; GFP-NL2-Thr, n = 210 nanoclusters) enrichment from neurons expressing GFP-NL2 (black) or GFP-NL2-Thr (cyan) following treatment with thrombin. (*H*) Enrichment indices (g_r < 50 nm) for $GABA_ARs$ across from RIM1/2 nanoclusters (black and cyan, *Left*; GFP-NL2, n = 417 nanoclusters; GFP-NL2-Thr, n = 522 nanoclusters. $P = 0.0014$) and RIM1/2 across from $GABA_ARs$ nanoclusters (black and orange, *Right*; GFP-NL2, n = 553 nanoclusters; GFP-NL2-Thr, n = 574 nanoclusters. $P = 0.0164$). (*I*) Schematic of the simulated expansion of synaptic clusters. (*J* and *K*) Effects of synaptic cluster expansion on the amplitudes of eIPSCs (*J*) and mIPSCs (*K*). (*L*) Pooled data of the impacts of synapse expansion on eIPSCs and mIPSCs. (*M*) Schematic of the simulated receptor dispersion from nanoclusters. (*N* and *O*) Effects of reduced receptor enrichment to release sites on the amplitudes of eIPSCs (*N*) and mIPSCs (*O*). (*P*) Pooled data of the impacts of receptor enrichment to release sites on eIPSCs and mIPSCs. (*Q*) Schematic of the simulated receptor reorganization similar with that resulting from NL2 cleavage. (*R* and *S*) Effects of receptor reorganization on eIPSC and eIPSC. (*T*) Pooled data of the simulated effects of structural changes observed in experiments on eIPSCs and mIPSCs. Each trace was averaged from 500 trials of simulations (*J*, *K*, *N*, *O*, *R*, *S*). *$P < 0.05$, **$P < 0.01$, ***$P < 0.001$. Significance was assessed with the Mann–Whitney test (*H*) and two-way ANOVA (*L*, *P*, and *T*).

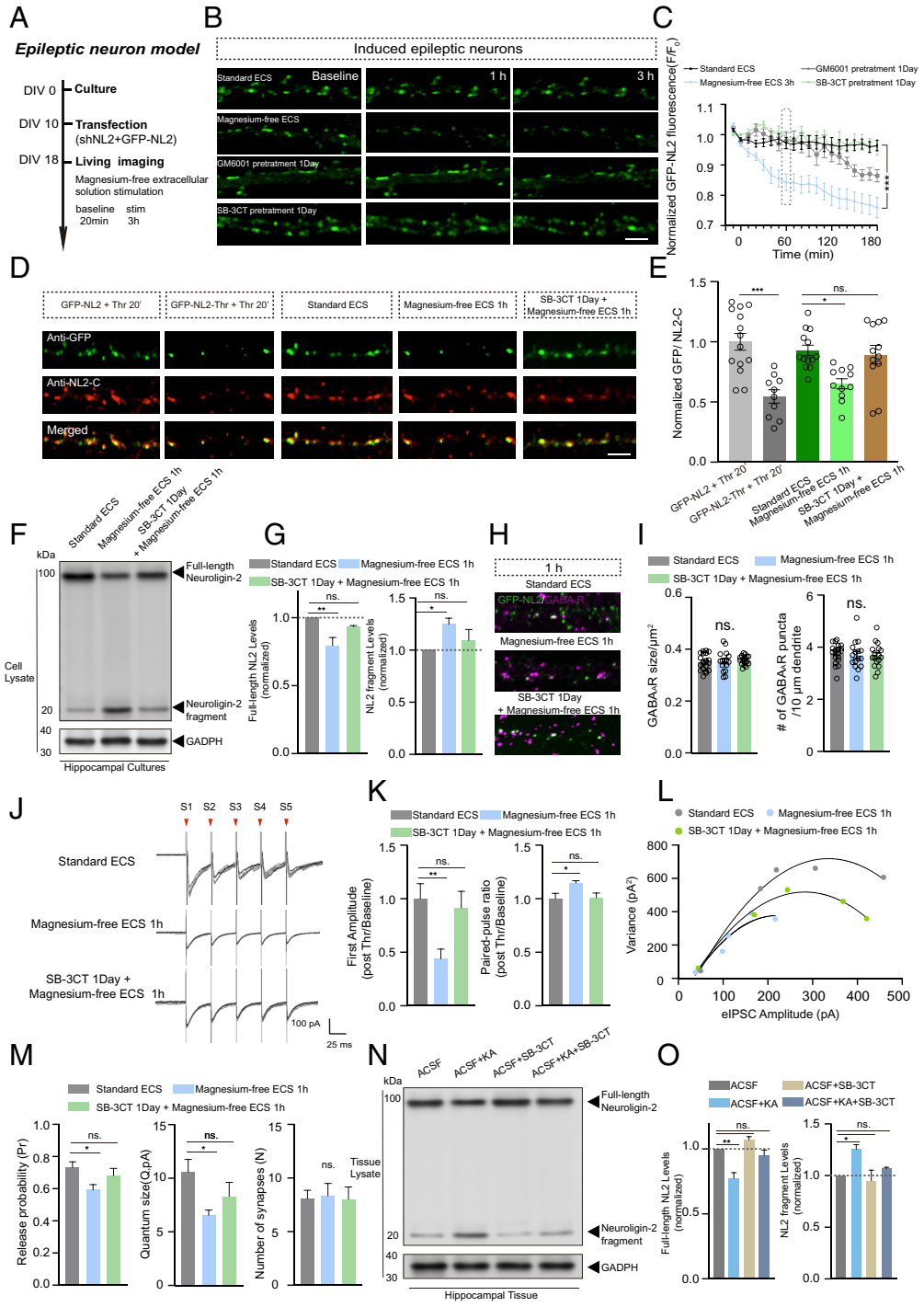

Fig. 7. NL2 is cleaved by MMP9 in response to increased neuronal activity. (*A*) Schematic timeline of magnesium-free extracellular solution-induced epileptic neuron model. (*B*) Representative images of neurons transfected with shNL2 and GFP-NL2 at three indicated time points in epileptic neuron models. (Scale bar, 5 μm.) (*C*) Normalized GFP-NL2 fluorescence (F/F0) along dendrites of transfected neurons in different groups. The dashed line box shows 1 h incubation in magnesium-free ECS. Standard ECS, n = 9 cells. Magnesium-free ECS, n = 12 cells. GM6001 pretreatment 1 d, n = 15 cells. SB-3CT pretreatment 1 d, n = 13 cells. $P < 0.0001$. $F_{(3,45)} = 12.9500$. (*D*) Representative fluorescent images of labeling targeting GFP and NL2-C tail in neurons transfected with GFP-NL2. (Scale bar, 5 μm.) (*E*) Pooled normalized ratio between GFP and NL2-C staining. GFP-NL2+Thr 20′, n = 14 cells; GFP-NL2-Thr+Thr 20′, n = 14 cells; standard ECS, n = 13 cells; Mg^{2+}-free ECS, n = 11 cells; GM6001 pretreatment, n = 12 cells. $P = 0.0001$. $P = 0.0124$. $P > 0.9999$. $F_{(4,42)} = 11.1500$. (*F*) Immunoblotting against NL2 in cell lysate probed with an antibody targeting C-terminus of NL2. (*G*) Pooled relative protein level for bands of full-length (*Left*) and C-terminus fragment (*Right*) of NL2. (*Left*), n = 3 cultures. $P = 0.0042$. $P = 0.1856$. (*Right*), n = 3 cultures. $P = 0.0278$. $P = 0.4633$. (*H*) Representative images of neurons coexpressing shNL2 and GFP-NL2 with immunostaining of endogenous $GABA_AR$. (Scale bar, 5 μm.) (*I*) Quantification of $GABA_AR$ puncta area (*Left*) and density (*Right*) in neurons in response to epilepsy induction. n = 20, 16, 17 cells for standard ECS, magnesium-free ECS, and SB-3CT pretreatment, respectively. (*J*) Representative IPSC traces triggered by five pulses with a 50 ms interval. Red arrows represent the stimulus. (Scale bar, 100 pA, 25 ms.) (*K*) Pooled normalized first-pulse amplitudes (*Left*) and PPR. Standard ECS, n = 14 cells; Mg^{2+}-free ECS, n = 15 cells; GM6001 pretreatment, n = 12 cells. (*Left*) $P = 0.0081$. $P > 0.9999$. $F_{(2,24)} = 6.5210$. (*Right*) $P = 0.0219$. $P > 0.9999$. $F_{(2,24)} = 5.3210$. (*L*) Fitting of the variance-amplitude relation for data from recordings in (*J*). (*M*) The release probability (*Left*), quantal size (*Middle*), and number of synapses (*Right*) derived from the parabolic fit. Standard ECS, n = 14 cells; Mg^{2+}-free ECS, n = 15 cells; GM6001 pretreatment, n = 12 cells. (*Left*), $P = 0.0362$, $P > 0.9999$. (*Middle*), $P = 0.0187$, $P = 0.3864$. (*Right*), $P > 0.9999$. (*N*) Immunoblotting against NL2 in tissue lysates. (*O*) Pooled relative protein level for bands of full-length (*Left*) and C-terminus fragment (*Right*) of NL2. (*Left*), n = 4 mice. $P = 0.0013$ and 0.5792. (*Right*), n = 4 mice. $P = 0.0448$ and 0.9999. All data are presented as the mean ± SEM. $^*P < 0.05$, $^{**}P < 0.01$, $^{***}P < 0.001$. Significance was assessed with two-way ANOVA with repeated measures (*C*) and one-way ANOVA with Bonferroni's post hoc test (*E*, *G*, *I*, *K*, *M*, and *O*).

These results strongly support our conclusion that MMP9-mediated cleavage of NL2 is enhanced during hyperactivation.

Discussion

In the current study, we used acute proteolysis of the NL2 ECD to illustrate the ongoing modulation of synaptic molecular nanoorganization and transmission by NL2-mediated transsynaptic interactions in mature GABAergic synapses. We found that acute cleavage of NL2 quickly led to a strong reduction in both postsynaptic quantum size and presynaptic neurotransmitter release probability. These functional changes were underlain by vigorous nanoscale redistribution of $GABA_A$Rs within the synapse, including an increase in PSD size and a reduction in local enrichment of receptors with sites of GABA release. More importantly, endogenous NL2 underwent MMP9-dependent cleavage in response to epileptic activities and decreased inhibitory synaptic transmission, suggesting a critical role of NL2 cleavage in mediating synaptic dysfunction in epileptic disorders.

Compared with conventional knockdown (46, 47) or conditional knockout approaches (30, 31), the acute proteolysis approach we employed in the current study has the advantage of high temporal resolution (15, 32) and provides unique information on the ongoing role of NL2 in established synapses at kinetic scales. There was strong nanoscale reorganization of $GABA_A$Rs (*SI Appendix*, Fig. S5 *A–G*) and gephyrin (*SI Appendix*, Fig. S8 *A–K*) as well as presynaptic RIM1/2 (Fig. 4 *A–K*) within synapses without changes in the synaptic retention of these proteins (*SI Appendix*, Fig. S5 *A–E*) immediately after the cleavage of NL2. The reorganization includes an expansion in volumes of both pre- and postsynaptic clusters and their subsynaptic nanoclusters. Therefore, NL2 is essential for the tight distribution of these synaptic proteins within synapses. The lack of immediate change in synaptic retention of $GABA_A$Rs or gephyrin within 1 h after NL2 cleavage is reflected in our finding that mIPSC amplitudes have only very small changes (Fig. 2*J*). This is also consistent with the well-established notion that gephyrin forms hexagonal submembranous lattice through strong oligomeric interactions (44). However, the cleavage of NL2 eventually produces a significant decrease in the stability of $GABA_A$Rs and gephyrin in synapses 12 to 24 h after cleavage (*SI Appendix*, Fig. S6 *A–H*), which is consistent with previous observations that loss of NL2 reduced clustering of gephyrin and GABA receptors (28). These results emphasize different roles of NL2-mediated interactions in the cleft in stabilizing postsynaptic protein organizations on different timescales. Meanwhile, since gephyrin spontaneously forms highly condensed molecular assemblies via phase separation on membrane bilayers when in complex with $GABA_A$Rs (48), NL2-mediated transsynaptic interactions could play a unique role in capturing these liquid condensates at right positions and controlling their sizes than stabilizing the inhibitory postsynaptic density itself.

Acute cleavage of postsynaptic NL2 rapidly leads to a reduction in release probability in presynaptic terminals (Fig. 3*I*), suggesting that NL2 cleavage acts as a transsynaptic retrograde signal. For AP-dependent transmitter release, the vesicle fusion sites are thought to be determined by nanoclusters of AZ scaffold proteins such as RIM (2, 3), and the release probability depends strongly on the abundance of Ca^{2+} channels as well as their local positioning (49, 50), especially relative to the docked vesicles (51). Our STORM results revealed a strong reorganization of RIM1/2 distribution in synapses with NL2 cleavage, including a volume expansion and a density decrease in both synaptic clusters and subsynaptic nanoclusters (Fig. 4 *E–K*). This may result from redistributions of presynaptic binding partners, such as neurexins and their interacting scaffolds, including CASK and Mint. The reduced local densities of RIM1/2 imply less-assembled release machinery or impaired local tethering of Ca^{2+} channels. We found no changes in either the presynaptic retention of Cav2.1 channels or their subsynaptic organization after the cleavage of NL2 (*SI Appendix*, Fig. S4 *A–O*), which argues against the possibility of altered Ca^{2+} channel tethering by NL2 disruption. However, with the high mobility of Ca^{2+} channels on the presynaptic membrane (52, 53), it is still possible that changes take place in a more dynamic way. Nevertheless, our observations based on acute thrombin-induced and activity-induced cleavage of NL2 support the notion that tuning NL-mediated transsynaptic interactions is an efficient way of regulating transmitter release.

Nanocolumns that align presynaptic transmitter release with postsynaptic receptor densities have been found in both excitatory (3) and inhibitory synapses (7, 17). Our results confirm the nanoscale enrichment between RIM1/2 and $GABA_A$Rs (Fig. 6*B*), and more importantly, NL2 is also enriched with $GABA_A$Rs (Fig. 6*D*). This implies the possibility that NL2 mediates the transsynaptic nanoalignment between the release machinery and $GABA_A$Rs. This is reasonable considering NL2 binds to presynaptic neurexins (54) and associates with postsynaptic $GABA_A$Rs through indirect interaction via gephyrin (29) and GARLH (55–57) as well as direct binding with α1-subunit (28, 58). Indeed, acute cleavage of NL2 significantly decreases the nanoscale enrichment between RIM1/2 and $GABA_A$Rs as well as gephyrin (Fig. 6 *F–H* and *SI Appendix*, Fig. S8 *I–K*), suggesting an essential role of NL2 in the maintenance of nanocolumns in inhibitory synapses. Multiple cleft molecules have been identified to participate in nanocolumn maintenance in excitatory synapses, including NL1 (13), LRRTM2 (15), and LGI1–ADAM22 (14) in hippocampal glutamatergic synapses, as well as NL3 (12) in the Held of Calyx. In the current study, we have demonstrated that NL2 participate in the constitution of transsynaptic nanocolumns in inhibitory synapses.

The nanocolumn-mediated release-receptor alignment is thought to determine the amplitude of the postsynaptic response in response to presynaptic single vesicle fusion, but the experimental evidence is very limited (13, 15, 17, 59). In the current study, we observed a larger reduction in evoked quantal size than mEPSCs (Fig. 3*J*) in response to acute cleavage of NL2. Spontaneous glutamate release from presynaptic terminals has been found to occur at different sites (3) and activate different postsynaptic receptors (8, 60) from evoked release. By assuming that spontaneous and evoked GABA release shares similarly distinct distributions of release sites in presynaptic terminals with glutamate release, we incorporated structural reorganization upon NL2 disruption in a numerical model of GABAergic synapses and fully replicated the changes in evoked and spontaneous quantal sizes in the electrophysiological recordings (Fig. 6 *Q–T*). These changes in synaptic transmission are well consistent with the observation in recent study that acutely repositioned $GABA_A$Rs within the postsynaptic membrane by optogenetic manipulating Gephyrin clustering (17). Our simulation predicted that the expansion of synaptic clusters and nanoclusters of receptors evenly reduces spontaneous and evoked quantal size, while the decrease in transsynaptic enrichment impacts only the evoked quantal size (Fig. 6 *I–P*), which is consistent with the simulations in glutamatergic synapses (12, 15). However, our simulation did not replicate the slower decay of IPSCs we have observed in electrophysiology, suggesting there may be other alterations after NL2 cleavage, such as gating properties of $GABA_A$Rs. Our experimental and numerical results have strengthened the notion that subsynaptic reorganization is an efficient regulator of synaptic strength (38) and provided evidence that specific aspects of subsynaptic nanoorganization play unique roles in modulating diverse synaptic functions.

The structural and functional alterations of synapses in response to acute cleavage of NL2 differ from those induced by acute

disruption of other adhesion molecules. Our experiments showed that acute cleavage of NL2 causes an expansion of synaptic clusters and nanoclusters for $GABA_A$Rs (Fig. 5 *A*–*G*), gephyrin (*SI Appendix*, Fig. S8 *A*–*K*), and RIM1/2 (Fig. 4 *E*–*K*) together with a reduction in release probability and quantal size of both evoked and spontaneous transmission (Fig. 6 *Q*–*T*). Similar proteolytic cleavage of NL1 in glutamatergic synapses alters presynaptic neurexin content and reduces presynaptic release probability (32) but has no effect on AMPAR organization (15) or mEPSC amplitude (32). However, acute cleavage of LRRTM2 prompts only the disorganization of AMPARs and specifically attenuates evoked EPSCs (15). Therefore, although these adhesion molecules share presynaptic binding partners, they play divergent roles in organizing synaptic molecular complexes and modulating synaptic functions.

Several classes of transsynaptic adhesion molecules are modulated by extracellularly acting proteases (61). Among these proteases, MMP9 has been extensively studied (62) and has been shown to cleave NL1 in a manner dependent on synaptic activity (32, 63). In line with these findings, our results demonstrate that NL2 undergoes rapid MMP-9-dependent cleavage in response to epileptic activities, as depicted in Fig. 7. This observation is consistent with previous studies showing upregulation and activation of MMP9 during seizures (64, 65). The MMP-9-mediated cleavage of NL2 leads to a notable decrease in inhibitory synaptic transmission. Our findings, in conjunction with previous work, provide substantial evidence supporting the idea that cleavage-induced nanostructural reorganization of NL2 plays a major role in synaptic dysfunction observed under hyperactive conditions. The impairment of inhibitory transmission could further contribute to the imbalance between excitation and inhibition in the circuitry, thereby exacerbating the occurrence of epilepsy. The acute proteolytic regulation of NL2, which we have elucidated in this study, holds significant implications for the pathophysiological mechanisms underlying synaptic dysfunction in epileptic disorders and may offer insights into therapeutic strategies.

Materials and Methods

Primary Cultures and Plasmids. All animal experiments were approved by the University of Science and Technology of China of the Animal Care and Use Committee requirements (approval no. USTCACUC1902024). The hippocampal neurons were prepared as previously described (66). For insertion of the thrombin cleavage site, a sequence coding the cleavage site (LTPRGVRL) with a flexible linker (GS) on the left side and a flexible linker (G) on the right side was inserted into the GFP-NL2 plasmid at position 2,845 ~ 2,846 bases from the sequence encoding the transmembrane domain. All subcloning was confirmed by sequencing. Gephyrin.FingR and PSD95.FingR were originally from Don Arnold Lab. Cultured neurons were transfected with an shRNA-containing plasmid shNL2-GFP (targeted sequences of mouse NL2 GGAGCAAGTTCAA CAGCAA), and GFP-NL2 or GFP-NL2-Thr at DIV9–10 (days in vitro) using a calcium phosphate transfection kit (Takara). All experiments were repeated on three or more separate cultures unless otherwise specified. Thrombin (Sigma-Aldrich, T6634) was added dropwise away from the objective into the imaging chamber with the final concentration of 10 U/mL.

STORM Immunocytochemistry and Imaging. The cell samples were fixed in 4% PFA and 4% sucrose in PBS for 10 min at room temperature (RT), followed by washing with PBS plus 50 mM glycine. Subsequently, the cells were incubated in blocking permeabilization buffer (5% BSA and 10% donkey serum in 0.3% Triton X-100), followed by incubation 3 h with primary antibody (rabbit anti-RIM1/2, Synaptic Systems, 140213, 1:400; Rabbit anti-CaV2.1, Synaptic Systems, 152203, 1:500; Mouse anti-Gephyrin, synaptic systems, 147021, 1:500; Guinea pig anti-$GABA_A$R γ2, synaptic systems, 224004, 1:500) at RT. Secondary antibodies (Donkey anti-Guinea Pig Alexa Fluor647, Jackson ImmunoResearch, 706-605-148, 1:200; Donkey anti-Rabbit Alexa Fluor647, Jackson ImmunoResearch, 711-605-152, 1:200; Donkey anti-Mouse Alexa Fluor647, Jackson ImmunoResearch, 715-605-151, 1:200; Cy3B, Mono NHS Ester, 16889934) were then applied for 1 h at RT. Imaging was performed on a Nikon ECLIPSE Ti2 inverted microscope equipped with a 100×/1.49 total internal reflection fluorescence oil-immersion objective controlled with Nikon software in a STORM imaging buffer containing 50 mM Tris, 10 mM NaCl, 20% glucose, 0.5 mg/mL glucose oxidase (Sigma), 18 μg/mL catalase (Sigma), and 100 mM cysteamine (Sigma). Emission was collected with a complementary metal–oxide semiconductor camera (ORCA-Flash4.0, Hamamatsu) at a frame rate of 50 Hz and stored as images with a pixel size of 160 nm. Detailed analyses on synaptic clusters were performed using custom routines in MATLAB as described previously (3).

Simulations. Release of GABA was carried out with MATLAB (version R2019a; MathWorks, Natick, MA) by using 3D free boundary condition solution (69) and dynamic binding to $GABA_A$Rs in a complex microenvironment with a time step of 0.5 μs. The spatiotemporal profile of GABA concentration in cleft after a vesicle fusion was described with Eq. **S4** (67).

$$[\mathrm{GABA}](d,t) = \left(\frac{M}{\alpha(4\pi D' t)}\right) e^{-\frac{d2}{4D' t}}. \qquad [\mathbf{S4}]$$

We adopted a previous model (68) to describe the kinetic states of $GABA_A$Rs. In the model, receptors can bind two molecules of agonist (*A*), leading to singly or doubly liganded closed (*C*), open (*O*), and desensitized (*D*) states. In response to rapid application of GABA, most of the current results from occupancy of OA_2, with a small contribution of OA at low concentrations of GABA. Based on the biexponential onset of desensitization, we included two doubly liganded desensitized states, the fast (DA_2f) and slow (DA_2s) desensitized states. Rate constants are given in *SI Appendix*, Table S2. The number of $GABA_A$Rs is varied from simulation to simulation in the range 0 to 100. Random receptors are distributed uniformly in the synaptic cluster while nanocluster receptors are distributed according to a normal distribution whose center is aligned with the center of the nanocolumn. Default parameters based on the data of STORM are given in *SI Appendix*, Tables S1 and S2. The traces shown here were mean values of 500 runs with release sites randomly distributed through the synaptic cluster for mIPSC and center of nanocluster for eIPSC. EPSC at time *t* is generated by

$$I(t) = \left[g \times n(t)\right] \times \left(V_m - V_{GABAAR}\right), \qquad [\mathbf{S5}]$$

where *g* is the single-channel conductance set at 27 ps, $n(t)$ is the number of open $GABA_A$Rs at time *t*, V_m is the resting membrane potential, and V_{GABAAR} is the reversal potential of $GABA_A$Rs.

Quantification and Statistical Analysis. The data analysis software used for all data processing was Fiji ImageJ, MATLAB2018b, Clampfit 10.7, and IgoPro software. The drawing software is Origin 9.60, GraphPad Prism 8, and Adobe Illustrator CC 2018. All data presented in this work were obtained from experimental replicates; neurons at least 3 times different hippocampal cell culture, three experimental repeats for each micrograph. Student's *t* test was used for simple comparison. One-way or two-way ANOVA with repeated measures and Bonferroni's post hoc analyses were used for multiparameter analysis. The K-S test was used for the frequency distribution graph. Significance levels are displayed as $^*P < 0.05$, $^{**}P < 0.01$, $^{***}P < 0.001$ and not significant (ns.), and the results are expressed as the mean ± SEM. *P* values are not provided as exact values when they were less than 0.0001.

Detailed methods can be found in *SI Appendix*.

Data, Materials, and Software Availability. Further information and requests for resources and reagents should be directed to and will be fulfilled by the lead contacts: Ai-Hui Tang(tangah@ustc.edu.cn). All materials and reagents used in this study are documented in Materials and Methods. All study data are included in the article and/or *SI Appendix*.

ACKNOWLEDGMENTS. This work was supported by STI2030-Major Projects (2021ZD0202503), the Strategic Priority Research Program of Chinese Academy of Sciences (XDB39010000), and the Fundamental Research Funds from from USTC (WK9110000141) and USTC Research Funds of the Double First-Class Initiative (YD9100002055) to A.-H.T. We thank Dr. Wei Lu in NIH/NINDS for providing the NL2 plasmids.

Author affiliations: [a]Department of Neurology, Institute on Aging and Brain Disorders, The First Affiliated Hospital, University of Science and Technology of China, Luyang District, Hefei, Anhui 230001, China; [b]Anhui Province Key Laboratory of Biomedical Imaging and Intelligent Processing, Institute of Artificial Intelligence, Hefei Comprehensive National Science Center, 5089 Wangjiang West Road, Gaoxin District, Hefei, Anhui 230088, China; [c]Ministry of Education Key Laboratory for Membrane-less Organelles and Cellular Dynamics, Division of Life Sciences and Medicine, University of Science and Technology of China, Shushan District, Hefei, Anhui 230027, China; [d]Hefei National Laboratory for Physical Sciences at the Microscale, Division of Life Sciences and Medicine, University of Science and Technology of China, Baohe District, Hefei, Anhui 230026, China; and [e]School of Life Sciences, Zhengzhou University, Zhengzhou, Henan 450001, China

1. T. C. Südhof, The cell biology of synapse formation. *J. Cell Biol.* **220**, e202103052 (2021).
2. H. Chen, A. H. Tang, T. A. Blanpied, Subsynaptic spatial organization as a regulator of synaptic strength and plasticity. *Curr. Opin. Neurobiol.* **51**, 147–153 (2018).
3. A. H. Tang *et al.*, A trans-synaptic nanocolumn aligns neurotransmitter release to receptors. *Nature* **536**, 210–214 (2016).
4. H. Sakamoto *et al.*, Synaptic weight set by Munc13-1 supramolecular assemblies. *Nat. Neurosci.* **21**, 41–49 (2018).
5. D. Nair *et al.*, Super-resolution imaging reveals that AMPA receptors inside synapses are dynamically organized in nanodomains regulated by PSD95. *J. Neurosci.* **33**, 13204–13224 (2013).
6. H. D. MacGillavry, Y. Song, S. Raghavachari, T. A. Blanpied, Nanoscale scaffolding domains within the postsynaptic density concentrate synaptic AMPA receptors. *Neuron* **78**, 615–622 (2013).
7. X. Yang, H. Le Corronc, P. Legendre, A. Triller, C. G. Specht, Differential regulation of glycinergic and GABAergic nanocolumns at mixed inhibitory synapses. *EMBO Rep.* **22**, e52154 (2021).
8. S. Li *et al.*, Asynchronous release sites align with NMDA receptors in mouse hippocampal synapses. *Nat. Commun.* **12**, 677 (2021).
9. A. Martinez-Sanchez *et al.*, Trans-synaptic assemblies link synaptic vesicles and neuroreceptors. *Sci. Adv.* **7**, eabe6204 (2021).
10. K. M. Franks, T. M. Bartol Jr., T. J. Sejnowski, A Monte Carlo model reveals independent signaling at central glutamatergic synapses. *Biophys. J.* **83**, 2333–2348 (2002).
11. S. Raghavachari, J. E. Lisman, Properties of quantal transmission at CA1 synapses. *J. Neurophysiol.* **92**, 2456–2467 (2004).
12. Y. Han *et al.*, Neuroligin-3 confines AMPA receptors into nanoclusters, thereby controlling synaptic strength at the calyx of Held synapses. *Sci. Adv.* **8**, eabo4173 (2022).
13. K. T. Haas *et al.*, Pre-post synaptic alignment through neuroligin-1 tunes synaptic transmission efficiency. *Elife* **7**, e31755 (2018).
14. Y. Fukata *et al.*, LGI1-ADAM22-MAGUK configures transsynaptic nanoalignment for synaptic transmission and epilepsy prevention. *Proc. Natl. Acad. Sci. U.S.A.* **118**, e2022580118 (2021).
15. A. M. Ramsey *et al.*, Subsynaptic positioning of AMPARs by LRRTM2 controls synaptic strength. *Sci. Adv.* **7**, eabf3126 (2021).
16. K. Nozawa *et al.*, In vivo nanoscopic landscape of neurexin ligands underlying anterograde synapse specification. *Neuron* **110**, 3168–3185.e8 (2022).
17. S. S. Olah *et al.*, Acute reorganization of postsynaptic GABA(A) receptors reveals the functional impact of molecular nanoarchitecture at inhibitory synapses. *Cell Rep.* **42**, 113331 (2023).
18. D. D. Krueger, L. P. Tuffy, T. Papadopoulos, N. Brose, The role of neurexins and neuroligins in the formation, maturation, and function of vertebrate synapses. *Curr. Opin. Neurobiol.* **22**, 412–422 (2012).
19. A. M. Craig, Y. Kang, Neurexin-neuroligin signaling in synapse development. *Curr. Opin. Neurobiol.* **17**, 43–52 (2007).
20. B. Chih, H. Engelman, P. Scheiffele, Control of excitatory and inhibitory synapse formation by neuroligins. *Science* **307**, 1324–1328 (2005).
21. E. R. Graf, X. Zhang, S. X. Jin, M. W. Linhoff, A. M. Craig, Neurexins induce differentiation of GABA and glutamate postsynaptic specializations via neuroligins. *Cell* **119**, 1013–1026 (2004).
22. K. Ichtchenko, T. Nguyen, T. C. Südhof, Structures, alternative splicing, and neurexin binding of multiple neuroligins. *J. Biol. Chem.* **271**, 2676–2682 (1996).
23. F. Varoqueaux, S. Jamain, N. Brose, Neuroligin 2 is exclusively localized to inhibitory synapses. *Eur. J. Cell Biol.* **83**, 449–456 (2004).
24. A. A. Chubykin *et al.*, Activity-dependent validation of excitatory versus inhibitory synapses by neuroligin-1 versus neuroligin-2. *Neuron* **54**, 919–931 (2007).
25. F. Varoqueaux *et al.*, Neuroligins determine synapse maturation and function. *Neuron* **51**, 741–754 (2006).
26. D. Krueger-Burg, T. Papadopoulos, N. Brose, Organizers of inhibitory synapses come of age. *Curr. Opin. Neurobiol.* **45**, 66–77 (2017).
27. J. Li *et al.*, Molecular dissection of neuroligin 2 and Slitrk3 reveals an essential framework for GABAergic synapse development. *Neuron* **96**, 808–826.e8 (2017).
28. A. Poulopoulos *et al.*, Neuroligin 2 drives postsynaptic assembly at perisomatic inhibitory synapses through gephyrin and collybistin. *Neuron* **63**, 628–642 (2009).
29. H. Ali, L. Marth, D. Krueger-Burg, Neuroligin-2 as a central organizer of inhibitory synapses in health and disease. *Sci. Signal.* **13**, eabd8379 (2020).
30. J. Liang *et al.*, Conditional neuroligin-2 knockout in adult medial prefrontal cortex links chronic changes in synaptic inhibition to cognitive impairments. *Mol. Psychiatry* **20**, 850–859 (2015).
31. E. Troyano-Rodriguez, C. R. Wirsig-Wiechmann, M. Ahmad, Neuroligin-2 determines inhibitory synaptic transmission in the lateral septum to optimize stress-induced neuronal activation and avoidance behavior. *Biol. Psychiatry* **85**, 1046–1055 (2019).
32. R. T. Peixoto *et al.*, Transsynaptic signaling by activity-dependent cleavage of neuroligin-1. *Neuron* **76**, 396–409 (2012).
33. R. M. Hines *et al.*, Synaptic imbalance, stereotypies, and impaired social interactions in mice with altered neuroligin 2 expression. *J. Neurosci.* **28**, 6055–6067 (2008).
34. Z. Fu, S. Vicini, Neuroligin-2 accelerates GABAergic synapse maturation in cerebellar granule cells. *Mol. Cell Neurosci.* **42**, 45–55 (2009).
35. E. T. Kavalali, The mechanisms and functions of spontaneous neurotransmitter release. *Nat. Rev. Neurosci.* **16**, 5–16 (2015).
36. R. S. Zucker, W. G. Regehr, Short-term synaptic plasticity. *Annu. Rev. Physiol.* **64**, 355–405 (2002).
37. R. A. Silver, Estimation of nonuniform quantal parameters with multiple-probability fluctuation analysis: Theory, application and limitations. *J. Neurosci. Methods* **130**, 127–141 (2003).
38. X. Z. Gou, A. M. Ramsey, A. H. Tang, Re-examination of the determinants of synaptic strength from the perspective of superresolution imaging. *Curr. Opin. Neurobiol.* **74**, 102540 (2022).
39. Y. Han, P. S. Kaeser, T. C. Südhof, R. Schneggenburger, RIM determines Ca^2+ channel density and vesicle docking at the presynaptic active zone. *Neuron* **69**, 304–316 (2011).
40. G. G. Gross *et al.*, Recombinant probes for visualizing endogenous synaptic proteins in living neurons. *Neuron* **78**, 971–985 (2013).
41. Y. Fukata *et al.*, Local palmitoylation cycles define activity-regulated postsynaptic subdomains. *J. Cell Biol.* **202**, 145–161 (2013).
42. K. C. Crosby *et al.*, Nanoscale subsynaptic domains underlie the organization of the inhibitory synapse. *Cell Rep.* **26**, 3284–97.e3 (2019).
43. S. K. Tyagarajan, J. M. Fritschy, Gephyrin: A master regulator of neuronal function? *Nat. Rev. Neurosci.* **15**, 141–156 (2014).
44. M. Sola *et al.*, Structural basis of dynamic glycine receptor clustering by gephyrin. *EMBO J.* **23**, 2510–2519 (2004).
45. J. H. Chen, T. A. Blanpied, A. H. Tang, Quantification of trans-synaptic protein alignment: A data analysis case for single-molecule localization microscopy. *Methods* **174**, 72–80 (2020).
46. K. Futai, C. D. Doty, B. Baek, J. Ryu, M. Sheng, Specific trans-synaptic interaction with inhibitory interneuronal neurexin underlies differential ability of neuroligins to induce functional inhibitory synapses. *J. Neurosci.* **33**, 3612–3623 (2013).
47. Q. A. Nguyen, M. E. Horn, R. A. Nicoll, Distinct roles for extracellular and intracellular domains in neuroligin function at inhibitory synapses. *Elife* **5**, e19236 (2016).
48. G. Bai, Y. Wang, M. Zhang, Gephyrin-mediated formation of inhibitory postsynaptic density sheet via phase separation. *Cell Res.* **31**, 312–325 (2021).
49. N. Holderith *et al.*, Release probability of hippocampal glutamatergic terminals scales with the size of the active zone. *Nat. Neurosci.* **15**, 988–997 (2012).
50. T. Miki *et al.*, Numbers of presynaptic Ca(2+) channel clusters match those of functionally defined vesicular docking sites in single central synapses. *Proc. Natl. Acad. Sci. U.S.A.* **114**, E5246–E5255 (2017).
51. Y. Nakamura *et al.*, Nanoscale distribution of presynaptic Ca(2+) channels and its impact on vesicular release during development. *Neuron* **85**, 145–158 (2017).
52. R. Schneider *et al.*, Mobility of calcium channels in the presynaptic membrane. *Neuron* **86**, 672–679 (2015).
53. J. Heck *et al.*, Transient confinement of Ca(V)2.1 Ca(2+)-channel splice variants shapes synaptic short-term plasticity. *Neuron* **103**, 66–79.e12 (2019).
54. T. C. Südhof, Synaptic neurexin complexes: A molecular code for the logic of neural circuits. *Cell* **171**, 745–769 (2017).
55. T. Yamasaki, E. Hoyos-Ramirez, J. S. Martenson, M. Morimoto-Tomita, S. Tomita, GARLH family proteins stabilize GABA(A) receptors at synapses. *Neuron* **93**, 1138–1152.e6 (2017).
56. E. C. Davenport *et al.*, An essential role for the tetraspanin LHFPL4 in the cell-type-specific targeting and clustering of synaptic GABA(A) receptors. *Cell Rep.* **21**, 70–83 (2017).
57. M. Wu *et al.*, Impairment of inhibitory synapse formation and motor behavior in mice lacking the NL2 binding partner LHFPL4/GARLH4. *Cell Rep.* **23**, 1691–1705 (2018).
58. M. Chen *et al.*, Blue native PAGE-antibody shift in conjunction with mass spectrometry to reveal protein subcomplexes: Detection of a cerebellar α1/α6-subunits containing γ-Aminobutyric acid type A receptor subtype. *Int. J. Mol. Sci.* **24**, 7632 (2023).
59. F. Pennacchietti *et al.*, Nanoscale molecular reorganization of the inhibitory postsynaptic density is a determinant of GABAergic synaptic potentiation. *J. Neurosci.* **37**, 1747–1756 (2017).
60. S. R. Metzbower, Y. Joo, D. R. Benavides, T. A. Blanpied, Properties of individual hippocampal synapses influencing NMDA-receptor activation by spontaneous neurotransmission. *eNeuro* **6**, ENEURO.0419-18.2019 (2019).
61. A. Gorlewicz, L. Kaczmarek, Pathophysiology of trans-synaptic adhesion molecules: Implications for epilepsy. *Front. Cell Dev. Biol.* **6**, 119 (2018).
62. G. W. Huntley, Synaptic circuit remodelling by matrix metalloproteinases in health and disease. *Nat. Rev. Neurosci.* **13**, 743–757 (2012).
63. K. Suzuki *et al.*, Activity-dependent proteolytic cleavage of neuroligin-1. *Neuron* **76**, 410–422 (2012).
64. J. W. Zhang, S. Deb, P. E. Gottschall, Regional and differential expression of gelatinases in rat brain after systemic kainic acid or bicuculline administration. *Eur. J. Neurosci.* **10**, 3358–3358 (1998).
65. G. M. Chen *et al.*, Important role of matrix metalloproteinase 9 in epileptogenesis. *J. Cell Biol.* **180**, 1021–1035 (2008).
66. J. H. Chen *et al.*, Reduced lysosomal density in neuronal dendrites mediates deficits in synaptic plasticity in Huntington's disease. *Cell Rep.* **42**, 113573 (2023).
67. E. M. Petrini *et al.*, Influence of GABAAR monoliganded states on GABAergic responses. *J. Neurosci.* **31**, 1752–1761 (2011).
68. J. R. Pugh, I. M. Raman, GABAA receptor kinetics in the cerebellar nuclei: Evidence for detection of transmitter from distant release sites. *Biophys. J.* **88**, 1740–1754 (2005).
69. B. Barbour, An evaluation of synapse independence. *J Neurosci*. 2001 Oct 15;**21**(20):7969-84. doi: 10.1523/JNEUROSCI.21-20-07969.2001. PMID: 11588170; PMCID: PMC6763864.